Available online at www.sciencedirect.com
SCIENCE DIRECT®
Journal of Sound and Vibration 263 (2003) 679–699
JOURNAL OF SOUND AND VIBRATION
www.elsevier.com/locate/jsvi

Letter to the Editor

Vibration of elevator cables with small bending stiffness

W.D. Zhu*, G.Y. Xu

Department of Mechanical Engineering, University of Maryland Baltimore County, 1000 Hilltop Circle, Baltimore, MD 21250, USA

Received 27 September 2002; accepted 3 October 2002

1. Introduction

While cables are employed in diverse engineering applications including suspension bridges [1], elevators [2], power transmission lines [3], and marine towing and mooring systems [4], they are subject to vibration due to their high flexibility and low intrinsic damping. Irvine and Caughey [5] and Triantafyllou [6] studied the dynamics of suspended cables with horizontal and inclined supports. Sergev and Iwan [7] and Cheng and Perkins [8] analyzed the vibration of cables with attached masses. Simpson [9], Triantafyllou [10], and Perkins and Mote [11] studied the in-plane and three-dimensional vibration of travelling cables. Wickert and Mote [12] and Zhu and Mote [13] analyzed the dynamic response of travelling cables with attached payloads. While the bending stiffness of cables is neglected in most studies, it was included in the models in Refs. [14,15] to avoid the singular behaviors associated with vanishing cable tension. Bending stiffness was also accounted for when cables are subjected to external moments [3,16] or when their local bending stresses need to be determined [17].

Vibration of elevator cables has been studied by several researchers [2,18–21]. Chi and Shu [2] calculated the natural frequencies associated with the longitudinal vibration of a stationary cable and car system. Roberts [18] used lumped mass approximations to model the longitudinal dynamics of hoist and compensation cables in high-rise elevators. Yamamoto et al. [19] analyzed the free and forced lateral vibration of a stationary string with slowly, linearly varying length. Terumichi et al. [20] examined the lateral vibration of a travelling string with slowly, linearly varying length and a mass-spring termination. Zhu and Ni [21] analyzed the dynamic stability of travelling media with variable length. The vibratory energy of the media was shown to decrease and increase in general during extension and retraction, respectively.

Due to its small bending stiffness relative to the tension, the moving hoist cable was modelled as a travelling string in Ref. [21]. By including the bending stiffness in the models for the stationary and moving hoist cables with different boundary conditions, the effects of bending stiffness and boundary conditions on their dynamic characteristics are investigated here. Convergence of the

*Corresponding author. Tel.: +1-410-455-3394; fax: +1-410-455-1052.
E-mail address: wzhu@umbc.edu (W.D. Zhu).

0022-460X/03/$ - see front matter
doi:10.1016/S0022-460X(02)01468-2

models is examined. The optimal stiffness and damping coefficient of the suspension of the car against its guide rails are identified for the moving cable.

2. Stationary cable models

2.1. Basic equations

We consider six models of the stationary hoist cable to evaluate the effects of bending stiffness and boundary conditions on its dynamic characteristics. Since the vertical cable has no sag, it is modelled as a taut string and a tensioned beam. Shown in Fig. 1 are the beam and string models of the cable with the suspension of the car against its guide rails assumed to be rigid. Shown in Fig. 2 are the beam and string models of the cable with the suspension of the car against the guide rails modelled by a resultant stiffness k_e and damping coefficient c_e. In all the cases the mass of the car is denoted by m_e. While the car can have finite dimensions in Fig. 1, it is modelled as a point mass in Fig. 2. When the cable is modelled as a tensioned beam, as shown in Figs. 1(a) and (b), and 2(a) and (b), its free lateral vibration in the xy plane is governed by

$$\rho y_{tt}(x,t) - [P(x)y_x(x,t)]_x + EIy_{xxxx}(x,t) = 0, \quad 0<x<l, \tag{1}$$

where the subscript denotes partial differentiation, $y(x,t)$ is the lateral displacement of the cable particle at position x at time t, l is the length of the cable, ρ is the mass per unit length, EI is the bending stiffness, and $P(x)$ is the tension at position x given by

$$P(x) = [m_e + \rho(l-x)]g, \tag{2}$$

in which g is the acceleration due to gravity. The boundary conditions of the cable with fixed ends, as shown in Fig. 1(a), are

$$y(0,t) = y_x(0,t) = 0, \quad y(l,t) = y_x(l,t) = 0. \tag{3}$$

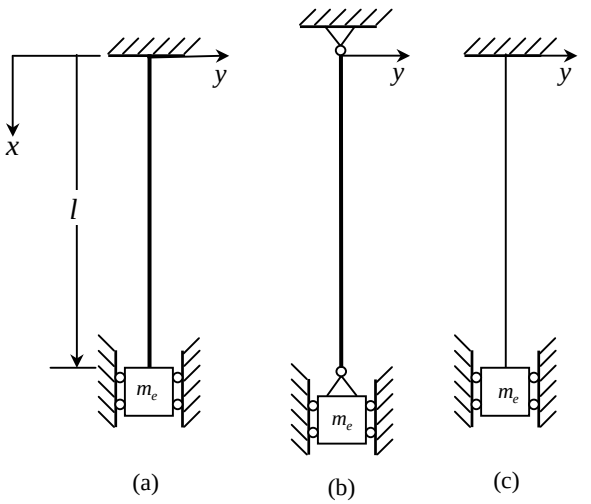

Fig. 1. Schematic of the stationary hoist cable with the suspension of the car against its guide rails assumed to be rigid: (a) fixed–fixed beam model, (b) pinned–pinned beam model, and (c) string model.

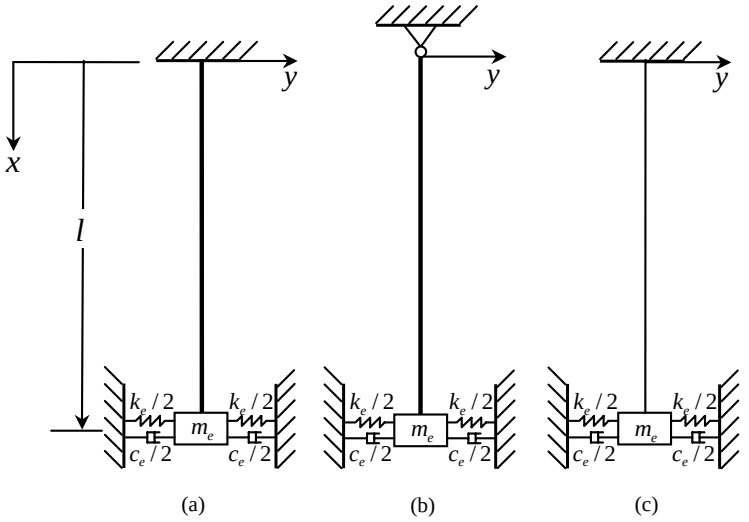

Fig. 2. Schematic of the stationary hoist cable where the car is modelled as a point mass m_e and its suspension against the guide rails has a resultant stiffness k_e and damping coefficient c_e: (a) beam model with a fixed end at $x = 0$, (b) beam model with a pinned end at $x = 0$, and (c) string model.

The boundary conditions of the cable with pinned ends, as shown in Fig. 1(b), are

$$y(0,t) = y_{xx}(0,t) = 0, \quad y(l,t) = y_{xx}(l,t) = 0. \tag{4}$$

For the cable models in Fig. 2(a) and (b), the boundary conditions at $x = 0$ are the same as those in Eqs. (3) and (4), respectively, and the boundary conditions at $x = l$ are

$$y_{xx}(l,t) = 0, \quad EIy_{xxx}(l,t) = P(l)y_x(l,t) + m_e y_{tt}(l,t) + c_e y_t(l,t) + k_e y(l,t). \tag{5}$$

Note that the bending moment at $x = l$ vanishes in the first equation in Eq. (5) because the rotary inertia of the car is not considered. The governing equation for the models in Figs. 1(c) and 2(c) is given by Eq. (1) with $EI = 0$, and the boundary condition at $x = 0$ is $y(0,t) = 0$. The boundary condition at $x = l$ for the model in Fig. 1(c) is $y(l,t) = 0$ and the boundary condition at $x = l$ for the model in Fig. 2(c) is given by the second equation in Eq. (5) with $EI = 0$. Due to vanishing slope of the cable at the fixed ends in Figs. 1(a) and 2(a), the models in Figs. 1(c) and 2(c) cannot be obtained from the models in Figs. 1(a) and 2(a), respectively, by setting $EI = 0$. In addition to providing a nominal tension $m_e g$, the mass of the car results in an inertial force in the second equation in Eq. (5) for the models in Fig. 2.

Galerkin's method and the assumed modes method are used to discretize the governing partial differential equations for the models in Figs. 1 and 2, respectively. The solution of Eq. (1) is assumed in the form

$$y(x,t) = \sum_{j=1}^{n} q_j(t)\phi_j(x), \tag{6}$$

where $\phi_j(x)$ are the trial functions, $q_j(t)$ are the generalized coordinates, and n is the number of included modes. The trial functions for the models in Fig. 1 satisfy all the boundary conditions and those for the models in Fig. 2 satisfy all the boundary conditions except the force boundary

condition in Eq. (5). Substituting Eq. (6) into Eq. (1) and the second equation in Eq. (5), multiplying the governing equation by $\phi_i(x)$ $(i = 1, 2, \ldots, n)$, integrating it from $x = 0$ to l, and using the resulting boundary condition yields the discretized equations for the models in Fig. 2(a) and (b):

$$\mathbf{M}\ddot{\mathbf{q}}(t) + \mathbf{C}\dot{\mathbf{q}}(t) + \mathbf{K}\mathbf{q}(t) = 0, \tag{7}$$

where $\mathbf{q} = [q_1, q_2, \ldots, q_n]^{\mathrm{T}}$ is the vector of generalized coordinates and $\mathbf{M}$, $\mathbf{K}$, and $\mathbf{C}$ are the symmetric mass, stiffness, and damping matrices, respectively, with entries

$$\mathbf{M}_{ij} = \int_0^l \rho\phi_i(x)\phi_j(x)\,\mathrm{d}x + m_e\phi_i(l)\phi_j(l), \tag{8}$$

$$\mathbf{K}_{ij} = \int_0^l P(x)\phi_i'(x)\phi_j'(x)\,\mathrm{d}x + \int_0^l EI\phi_i''(x)\phi_j''(x)\,\mathrm{d}x + k_e\phi_i(l)\phi_j(l), \tag{9}$$

$$\mathbf{C}_{ij} = c_e\phi_i(l)\phi_j(l), \tag{10}$$

in which the prime denotes differentiation with respect to x. The discretized equations for the model in Fig. 2(c) are given by Eqs. (7)–(10) with $EI = 0$ in Eq. (9). The discretized equations for the models in Fig. 1(a) and (b) are given by Eqs. (7)–(10) with $m_e = 0$ in Eq. (8) and $k_e = c_e = 0$ in Eqs. (9) and (10); the discretized equations for the model in Fig. 1(c) are given by Eqs. (7)–(10) with $m_e = 0$ in Eq. (8) and $k_e = EI = c_e = 0$ in Eqs. (9) and (10). While the discretized equations for the models in Fig. 1(a) and (b) have the same form, the trial functions used satisfy different boundary conditions. This also holds for the models in Fig. 2(a) and (b).

The eigenfunctions of a fixed–fixed beam and those of a fixed–fixed beam under uniform tension $T = m_e g$ are used as the trial functions for the model in Fig. 1(a). The eigenfunctions of a pinned–pinned beam, which are identical to those of a pinned–pinned beam under uniform tension, are used as the trial functions for the model in Fig. 1(b). The eigenfunctions of a fixed–fixed string, which are identical to those of a pinned–pinned beam, are used as the trial functions for the model in Fig. 1(c). Due to the same trial functions the discretized equations for the model in Fig. 1(c) can be obtained from those for the model in Fig. 1(b) by setting $EI = 0$. The eigenfunctions of a cantilever beam and those of a fixed–free beam under uniform tension $T = m_e g$ are used as the trial functions for the model in Fig. 2(a). The eigenfunctions of a pinned–free beam and those of a pinned–free beam under uniform tension $T = m_e g$ are used as the trial functions for the model in Fig. 2(b). The eigenfunctions of a fixed–free string are used as the trial functions for the model in Fig. 2(c). Note that a pinned–free beam has a rigid-body mode and a fixed–free string does not. The discretized equations for the model in Fig. 2(c) cannot be obtained as a special case from those for the model in Fig. 2(b) due to the different trial functions used. All the trial functions are normalized and given in Appendix A. By the orthogonality relations the mass matrix for the models in Fig. 1 is a diagonal matrix. If the initial displacement and velocity of the cable in Figs. 1 and 2 are given by $y(x, 0)$ and $y_t(x, 0)$, respectively, the initial conditions for the generalized coordinates are

$$q_j(0) = \int_0^l \phi_j(x)y(x, 0)\,\mathrm{d}x, \quad \dot{q}_j(0) = \int_0^l \phi_j(x)y_t(x, 0)\,\mathrm{d}x. \tag{11}$$

The energy of the models in Fig. 1(a) and (b) is

$$E_v(t) = \frac{1}{2}\int_0^l (\rho y_t^2 + P y_x^2 + EI y_{xx}^2)\,\mathrm{d}x \tag{12}$$

and that of the models in Fig. 2(a) and (b) is

$$E_v(t) = \frac{1}{2}\int_0^l (\rho y_t^2 + P y_x^2 + EI y_{xx}^2)\,\mathrm{d}x + \tfrac{1}{2} m_e y_t^2(l,t) + \tfrac{1}{2} k_e y^2(l,t). \tag{13}$$

The energy of the models in Figs. 1(c) and 2(c) is given by Eqs. (12) and (13), respectively, with $EI = 0$. Substituting Eq. (6) into Eqs. (12) and (13) yields the discretized energy expression for the models in Figs. 1 and 2:

$$E_v(t) = \tfrac{1}{2}[\dot{\mathbf{q}}^{\mathrm{T}}(t)\mathbf{M}\dot{\mathbf{q}}(t) + \mathbf{q}^{\mathrm{T}}(t)\mathbf{K}\mathbf{q}(t)], \tag{14}$$

where $\mathbf{M}$ and $\mathbf{K}$ are the corresponding mass and stiffness matrices. Differentiating Eqs. (12) and (13) and using the governing equations and boundary conditions yields $\dot{E}_v(t) = 0$ for the models in Fig. 1 and $\dot{E}_v(t) = -c_e y_t^2(l,t)$ for the models in Fig. 2. The discretized expression of $\dot{E}_v(t)$ for the models in Fig. 2 is $\dot{E}_v(t) = -\dot{\mathbf{q}}^{\mathrm{T}}(t)\mathbf{C}\dot{\mathbf{q}}(t)$.

2.2. Results and discussion

The parameters used here are similar to those in Refs. [21,22]: $\rho = 1.005\,\mathrm{kg/m}$, $EI = 1.39\,\mathrm{N\,m^2}$, $m_e = 756\,\mathrm{kg}$, $g = 9.81\,\mathrm{m/s^2}$, $l = 171\,\mathrm{m}$, and $k_e = 2083\,\mathrm{N/m}$. The undamped natural frequencies, ω_i, and modes, $\mathbf{x}_i$, of the system in Eq. (7) are obtained from the eigenvalue problem, $\mathbf{K}\mathbf{x}_i = \omega_i^2\mathbf{M}\mathbf{x}_i$ $(i = 1, 2, \ldots, n)$. Using the aforementioned trial functions and various numbers of terms in Eq. (6), the first three natural frequencies of the models in Figs. 1 and 2 are calculated as shown in Table 1. The trial functions for the models in Figs. 1(a), and 2(a) and (b), corresponding to $T = m_e g$ and $T = 0$, are referred to as the tensioned and untensioned beam eigenfunctions, respectively. As the natural frequencies converge from above, the use of the tensioned beam eigenfunctions significantly accelerates the convergence of the natural frequencies of the model in Fig. 1(a). The untensioned beam eigenfunctions yield improved estimates of the natural frequencies of the models in Fig. 2(a) and (b) for $n > 1$. Due to the rotational constraints at the fixed ends the natural frequencies of the models in Figs. 1(a) and 2(a) are slightly higher than those of the models in Figs. 1(b) and 2(b), respectively. Due to small bending stiffness the natural frequencies of the model in Fig. 1(b) are identical to those of the model in Fig. 1(c) within the accuracy shown for all n. The natural frequencies of the models in Fig. 1(b) and (c) converge at similar rates as the natural frequencies of the model in Fig. 1(a) using the tensioned beam eigenfunctions. The natural frequencies of the model in Fig. 2(c) converge at similar rates as the natural frequencies of the models in Fig. 2(a) and (b) using the tensioned beam eigenfunctions. The natural frequencies of the models in Fig. 2 approach those of the corresponding models in Fig. 1 when k_e approaches infinity.

Consider the undamped (i.e., $c_e = 0$) responses of the models in Figs. 1 and 2 to the initial displacements given in Appendix B and zero initial velocity. The initial displacement for the models in Figs. 1(a) and 2(a) is the static deflection of a fixed–fixed beam under uniform tension $m_e g$, subjected to a concentrated force at $x = a$ resulting in a displacement d at $x = a$. The initial

Table 1
The first three natural frequencies (in rad/s) of the models in Figs. 1 and 2 calculated using different numbers of terms in Eq. (6), where T is the tension of the beams whose eigenfunctions are used as the trial functions for the models in Figs. 1(a), and 2(a) and (b)

Number of modes n			1	2	3	10	20	30	50	100	150
Fig. 1(a)	$T=0$	1st	1.859	1.858	1.774	1.710	1.687	1.679	1.673	1.668	1.666
		2nd		3.598	3.596	3.412	3.372	3.358	3.345	3.336	3.333
		3rd			5.303	5.128	5.061	5.038	5.019	5.004	5.000
	$T=m_eg$	1st	1.666	1.664	1.664	1.664	1.664	1.664	1.664	1.664	1.664
		2nd		3.333	3.328	3.328	3.328	3.328	3.328	3.328	3.328
		3rd			5.002	4.991	4.991	4.991	4.991	4.991	4.991
Fig. 1(b)		1st	1.665	1.663	1.663	1.663	1.663	1.663	1.663	1.663	1.663
		2nd		3.332	3.327	3.327	3.327	3.327	3.327	3.327	3.327
		3rd			5.000	4.990	4.990	4.990	4.990	4.990	4.990
Fig. 1(c)		1st	1.665	1.663	1.663	1.663	1.663	1.663	1.663	1.663	1.663
		2nd		3.332	3.327	3.327	3.327	3.327	3.327	3.327	3.327
		3rd			5.000	4.990	4.990	4.990	4.990	4.990	4.990
Fig. 2(a)	$T=0$	1st	1.636	1.533	1.532	1.506	1.501	1.499	1.498	1.497	1.496
		2nd		1.898	1.887	1.851	1.844	1.842	1.840	1.838	1.838
		3rd			3.480	3.397	3.374	3.366	3.360	3.355	3.354
	$T=m_eg$	1st	1.596	1.559	1.539	1.510	1.503	1.500	1.499	1.497	1.497
		2nd		1.986	1.917	1.857	1.847	1.844	1.841	1.839	1.838
		3rd			3.671	3.424	3.387	3.375	3.365	3.358	3.356
Fig. 2(b)	$T=0$	1st	1.619	1.509	1.498	1.496	1.496	1.496	1.496	1.496	1.496
		2nd		1.840	1.837	1.837	1.837	1.837	1.837	1.837	1.837
		3rd			3.398	3.351	3.351	3.351	3.351	3.351	3.351
	$T=m_eg$	1st	1.596	1.559	1.539	1.510	1.503	1.500	1.498	1.497	1.497
		2nd		1.985	1.917	1.857	1.847	1.843	1.841	1.839	1.838
		3rd			3.670	3.424	3.386	3.374	3.365	3.358	3.355
Fig. 2(c)		1st	1.596	1.559	1.539	1.510	1.503	1.500	1.498	1.497	1.497
		2nd		1.985	1.917	1.857	1.847	1.843	1.841	1.839	1.838
		3rd			3.670	3.424	3.386	3.374	3.365	3.358	3.355

displacement for the models in Figs. 1(b) and 2(b) is the static deflection of a pinned–pinned beam under the same tension, subjected to a concentrated force at $x=a$ resulting in a displacement d at $x=a$. The initial displacement for the models in Figs. 1(c) and 2(c) is the static deflection of a fixed–fixed string subjected to a concentrated force at $x=a$ with a displacement d at $x=a$. The above initial displacements for $a=100\,\mathrm{m}$ and $d=0.07\,\mathrm{m}$ are shown in Fig. 3; the resulting displacements and velocities of a particle of the models in Figs. 1 and 2 at $x=156\,\mathrm{m}$ are shown in Figs. 4 and 5, respectively, for $0\leqslant t\leqslant t_f=38\,\mathrm{s}$, where t_f is the final time of the moving cable in Section 3.2. Note that the small bending stiffness leads to the boundary layers in the deflections of the beams in the vicinity of the fixed ends and concentrated force to ensure satisfaction of the boundary and internal conditions. Due to small bending stiffness the responses of the models in

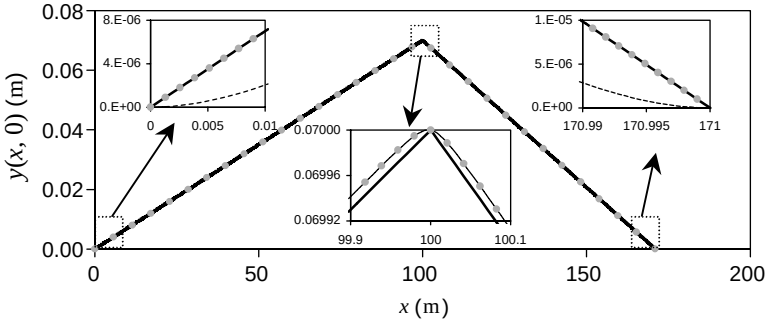

Fig. 3. The initial displacements for the models in: Figs. 1(a) and 2(a) (dashed lines); Figs. 1(b) and 2(b) (dots); Figs. 1(c) and 2(c) (solid lines). The boundary layers are shown in dashed lines in the expanded views near the boundaries and dashed lines and dots in the expanded view near $x = 100$ m.

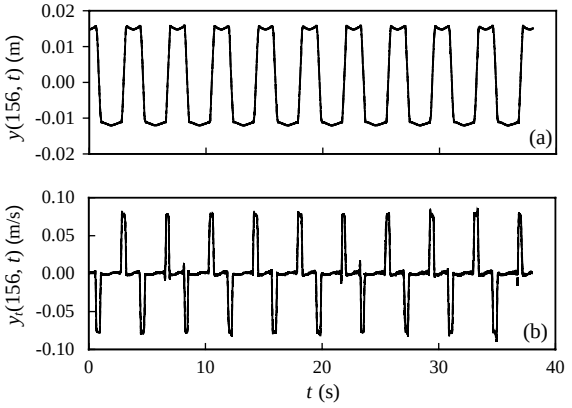

Fig. 4. The displacement (a) and velocity (b) of the particle at $x = 156$ m in the models in Fig. 1 under the corresponding initial displacements shown in Fig. 3: dashed lines, Fig. 1(a); dash–dotted lines, Fig. 1(b); solid lines, Fig. 1(c). The energies of the models are shown in Fig. 11(a). The tensioned beam eigenfunctions are used for the response of the model in Fig. 1(a) and $n = 30$ in all the cases.

Figs. 1 and 2 are virtually indistinguishable within the scales of the plots in Figs. 4 and 5, respectively. While the maximum displacement in Fig. 5 is larger than that in Fig. 4, the energies shown by the horizontal lines in Figs. 11(a) and 12(a) are essentially the same. Convergence of the responses of the various models is similar to that of the natural frequencies discussed earlier.

Under the above initial conditions the transverse force at the lower end (i.e., $x = l$) of each model in Fig. 1 is shown in Fig. 6(a). While the transverse force at $x = l$ is given by the shear force $-EIy_{xxx}(l, t)$ for the model in Fig. 1(a) because $y_x(x, l) = 0$, by the transverse component of the tension $P(l)y_x(l, t)$ for the model in Fig. 1(c), and by both terms $-EIy_{xxx}(l, t) + P(l)y_x(l, t)$ for the model in Fig. 1(b), it has essentially the same value for the three models. The bending moment at the lower end of the model in Fig. 1(a) is shown in Fig. 6(b); the bending moment at the two ends of the model in Fig. 1(b) vanishes identically. The bending moment at an interior point (e.g., $x = 156$ m) of the models in Fig. 1(a) and (b) has an amplitude that is orders of magnitude smaller

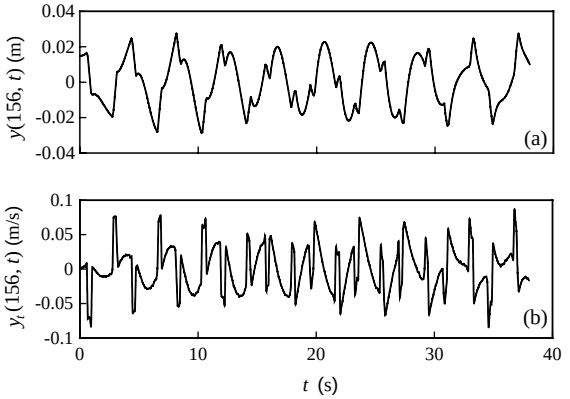

Fig. 5. The displacement (a) and velocity (b) of the particle at $x = 156$ m in the models in Fig. 2 under the corresponding initial displacements shown in Fig. 3: dashed lines, Fig. 2(a); dash-dotted lines, Fig. 2(b); solid lines, Fig. 2(c). The energies of the models are shown in Fig. 12(a). The untensioned beam eigenfunctions are used for the models in Fig. 2(a) and (b) and $n = 30$ in all the cases.

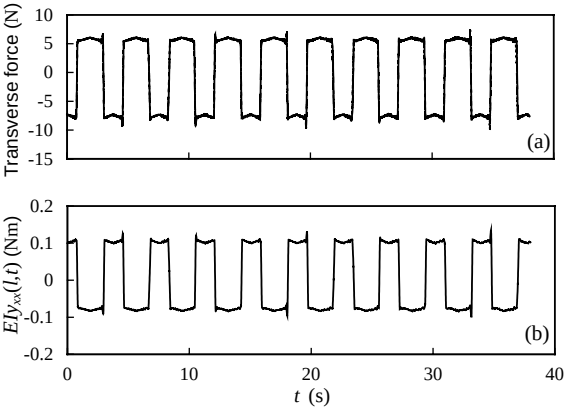

Fig. 6. (a) The transverse force at the lower end of each model in Fig. 1 under the corresponding initial displacement shown in Fig. 3: dashed lines, Fig. 1(a); dash-dotted lines, Fig. 1(b); solid lines, Fig. 1(c). (b) The bending moment at the upper end of the model in Fig. 1(a). The tensioned beam eigenfunctions are used for the model in Fig. 1(a) and $n = 100$ in all the cases.

than those at the fixed ends of the model in Fig. 1(a). Only the tensioned beam eigenfunctions can be used to estimate the bending moment and shear force at the fixed ends of the model in Fig. 1(a); the untensioned beam eigenfunctions will lead to slowly convergent series for the higher order derivatives, y_{xx} and y_{xxx}. Both the tensioned and untensioned beam eigenfunctions can be used to determine the transverse force at an interior point of the model in Fig. 1(a) and any point of the model in Fig. 1(b) because it is dominated by the transverse component of the tension, which involves the first order derivative y_x. The transverse force and bending moment are related to the transverse and bending stresses, respectively, in the analysis of cumulative fatigue damage.

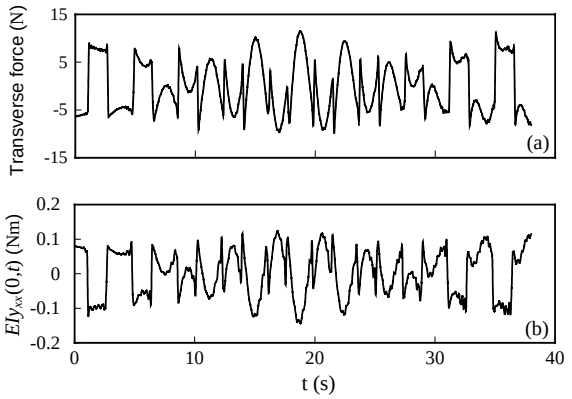

Fig. 7. (a) The transverse force at the upper end of each model in Fig. 2 under the corresponding initial displacement shown in Fig. 3: dashed lines, Fig. 2(a); dash–dotted lines, Fig. 2(b); solid lines, Fig. 2(c). (b) The bending moment at the upper end of the model in Fig. 2(a). In all the cases $n = 100$.

Under the above initial conditions the transverse force at the upper end (i.e., $x = 0$) of each model in Fig. 2 is shown in Fig. 7(a). Similar to the case in Fig. 6(a), the transverse force at $x = 0$, though given by different expressions, has essentially the same value for the three models. The bending moment at the upper end of the model in Fig. 2(a) is shown in Fig. 7(b). Note that the eigenfunctions of a fixed–free beam under uniform tension $T = m_e g + \rho g l$, which is the cable tension at $x = 0$, are used to calculate the shear force and bending moment at the upper end of the model in Fig. 2(a). Both the tensioned and untensioned beam eigenfunctions can be used to calculate the transverse force at an interior point of the model in Fig. 2(a) and any point of the model in Fig. 2(b). Only the untensioned beam eigenfunctions can be used to determine the transverse force at the lower end of the models in Fig. 2(a) and (b) because they satisfy a more realistic boundary condition, $EIy_{xxx}(l,t) = 0$, than the tensioned beam eigenfunctions, $EIy_{xxx}(l,t) = Ty_x(l,t)$. The transverse force at the lower end of the model in Fig. 2(c) cannot be determined here because the trial functions satisfy $\phi_j'(l) = 0$.

3. Moving cable models

3.1. Basic equations

Shown in Figs. 8 and 9 are the six models of the moving hoist cable corresponding to the stationary cable models in Figs. 1 and 2. During its motion the cable has a variable length $l(t)$ and an axial velocity $v(t) = \dot{l}(t)$. When the cable is modelled as a travelling tensioned beam, as shown in Figs. 8(a) and (b), and 9(a) and (b), its free lateral vibration relative to the fixed coordinate system, xy, is governed by [21]

$$\rho \frac{\mathrm{D}^2 y(x,t)}{\mathrm{D}t^2} - [P(x,t)y_x(x,t)]_x + EIy_{xxxx}(x,t) = 0, \quad 0 < x < l(t), \tag{15}$$

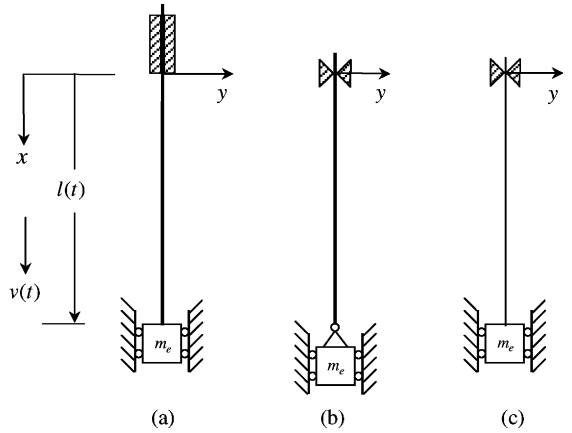

Fig. 8. Schematic of the moving hoist cable with the suspension of the car against its guide rails assumed to be rigid: (a)–(c) as in Fig. 1.

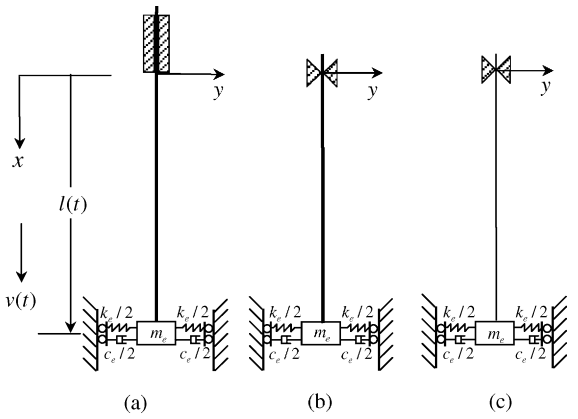

Fig. 9. Schematic of the moving hoist cable where the car is modelled as a point mass m_e and its suspension against the guide rails has a resultant stiffness k_e and damping coefficient c_e: (a)–(c) as in Fig. 2.

where

$$\frac{\mathrm{D}^2}{\mathrm{D}t^2} = \frac{\partial^2}{\partial t^2} + 2v(t)\frac{\partial^2}{\partial x\,\partial t} + v^2(t)\frac{\partial^2}{\partial x^2} + \dot{v}(t)\frac{\partial}{\partial x}, \tag{16}$$

$y(x,t)$ is the lateral displacement of the cable particle instantaneously located at position x at time t, $P(x,t)$ is the tension given by

$$P(x,t) = [m_e + \rho(l(t) - x)][g - \dot{v}(t)], \tag{17}$$

and the other variables are defined in Section 2.1. The governing equation for the models in Figs. 8(c) and 9(c) is given by Eq. (15) with $EI = 0$. The boundary conditions for each model in Figs. 8 and 9 are given by those for the corresponding stationary cable model in Section 2.1 with l

replaced with $l(t)$ and $P(l)$, $y_t(l,t)$ and $y_{tt}(l,t)$ in Eq. (5) replaced with $P(l(t),t)$, $\mathrm{D}y(l(t),t)/\mathrm{D}t$ and $\mathrm{D}^2y(l(t),t)/\mathrm{D}t^2$, respectively, where $\mathrm{D}/\mathrm{D}t = y_t + v(t)y_x$ and $\mathrm{D}^2/\mathrm{D}t^2$ is defined in Eq. (16). The models in Figs. 8(c) and 9(c) cannot be obtained as a special case from the models in Figs. 8(a) and 9(a), respectively. The mass of the car provides a tension $m_e(g-\dot{v})$ and an inertial force in the force boundary condition for the models in Fig. 9.

Galerkin's method and the assumed modes method are modified to discretize the governing partial equations for the models in Figs. 8 and 9, respectively. The solution of Eq. (15) is assumed in the form

$$y(x,t) = \sum_{j=1}^{n} q_j(t)\phi_j(x,t), \tag{18}$$

where $\phi_j(x,t)$ are the time-dependent trial functions and the other variables are defined in Section 2.1. Following Ref. [21] the instantaneous eigenfunctions of stationary beams and strings with variable length $l(t)$ are used as the trial functions for the models in Figs. 8 and 9. They satisfy the same boundary conditions as the trial functions for the corresponding stationary cable models in Section 2.1 and are normalized so that $\int_0^{l(t)} \phi_j^2(x,t)\,\mathrm{d}x = 1$. Note that the trial functions for the model in Fig. 9(b) contain a rigid-body mode. Because the trial functions for each model can be expressed as [21,22]

$$\phi_j(x,t) = \frac{1}{\sqrt{l(t)}}\psi_j(\xi), \tag{19}$$

where $\xi = x/l(t)$ and $\psi_j(\xi)$, given in Appendix A, are the normalized eigenfunctions of the corresponding stationary beam or string with unit length, dependence of the system matrices in Eq. (20) on time appears in the coefficient of their component matrices, which greatly simplifies the analysis. The normalized, instantaneous eigenfunctions of the tensioned beams with variable length $l(t)$ cannot be decomposed in the same manner as Eq. (19) and are not used as the trial functions for the models in Figs. 8(a), and 9(a) and (b). Substituting Eqs. (18) and (19) into Eq. (15) and the force boundary condition at $x = l(t)$, multiplying the governing equation by $\psi_i(\xi)/\sqrt{l(t)}$, integrating it from $x = 0$ to $l(t)$, and using the resulting boundary condition and the orthonormality relations for $\psi_j(\xi)$ yields the discretized equations for the models in Fig. 9(a) and (b):

$$\mathbf{M}(t)\ddot{\mathbf{q}}(t) + [\mathbf{C}(t) + \mathbf{G}(t)]\dot{\mathbf{q}}(t) + [\mathbf{K}(t) + \mathbf{H}(t)]\mathbf{q}(t) = 0, \tag{20}$$

where entries of the symmetric mass, stiffness, and damping matrices are

$$\mathbf{M}_{ij} = \rho\delta_{ij} + m_e l^{-1}(t)\psi_i(1)\psi_j(1), \tag{21}$$

$$\begin{aligned}\mathbf{K}_{ij} = {} & \tfrac{1}{4}\rho l^{-2}(t)\dot{l}^2(t)\delta_{ij} - \rho l^{-2}(t)\dot{l}^2(t)\int_0^1 (1-\xi)^2\psi_i'(\xi)\psi_j'(\xi)\,\mathrm{d}\xi + \rho l^{-1}(t)[g-\ddot{l}(t)]\int_0^1 (1-\xi)\psi_i'(\xi)\psi_j'(\xi)\,\mathrm{d}\xi \\ & + m_e l^{-2}(t)[g-\ddot{l}(t)]\int_0^1 \psi_i'(\xi)\psi_j'(\xi)\,\mathrm{d}\xi + EIl^{-4}(t)\int_0^1 \psi_i''(\xi)\psi_j''(\xi)\,\mathrm{d}\xi \\ & + [m_e\left(\tfrac{3}{4}\dot{l}^2(t)l^{-3}(t) - \tfrac{1}{2}\ddot{l}(t)l^{-2}(t)\right) - \tfrac{1}{2}c_e l^{-2}(t)\dot{l}(t) + k_e l^{-1}(t)]\psi_i(1)\psi_j(1),\end{aligned} \tag{22}$$

$$\mathbf{C}_{ij} = c_e l^{-1}(t)\psi_i(1)\psi_j(1) - m_e l^{-2}(t)\dot{l}(t)\psi_i(1)\psi_j(1), \tag{23}$$

in which δ_{ij} is the Kronecker delta, and entries of the skew-symmetric gyroscopic and circulatory matrices are

$$\mathbf{G}_{ij} = \rho l^{-1}(t)\dot{l}(t)\left[2\int_0^1 (1-\xi)\psi_i(\xi)\psi_j'(\xi)\,\mathrm{d}\xi - \delta_{ij}\right], \tag{24}$$

$$\mathbf{H}_{ij} = \rho[l^{-2}(t)\dot{l}^2(t) - l^{-1}(t)\ddot{l}(t)]\left[\tfrac{1}{2}\delta_{ij} - \int_0^1 (1-\xi)\psi_i(\xi)\psi_j'(\xi)\,\mathrm{d}\xi\right]. \tag{25}$$

The discretized equations for the model in Fig. 9(c) are given by Eqs. (20)–(25) with $EI = 0$ in Eq. (22). The discretized equations for the models in Fig. 8(a) and (b) are given by Eqs. (20)–(25) with $m_e = 0$ in Eq. (21), the last term involving $\psi_i(1)\psi_j(1)$ in Eq. (22) set to zero, and $c_e = m_e = 0$ in Eq. (23). The discretized equations for the model in Fig. 8(c) are given by those for the models in Fig. 8(a) and (b) with $EI = 0$ in the entries of $\mathbf{K}$. The discretized equations for the model in Fig. 8(c) can be obtained from those for the model in Fig. 8(b) by setting $EI = 0$; the discretized equations for the model in Fig. 9(c) cannot be obtained as a special case from those for the model in Fig. 9(b). If the initial displacement and velocity of the cable in Figs. 8 and 9 are given by $y(x,0)$ and $y_t(x,0)$, respectively, where $0<x<l(0)$, the initial conditions for the generalized coordinates are

$$q_j(0) = \sqrt{l(0)}\int_0^1 y(\xi l(0),0)\psi_j(\xi)\,\mathrm{d}\xi, \tag{26}$$

$$\dot{q}_j(0) = \sqrt{l(0)}\int_0^1 y_t(\xi l(0),0)\psi_j(\xi)\,\mathrm{d}\xi + \frac{v(0)}{l(0)}\sum_{i=1}^{n} q_i(0)\int_0^1 \xi\psi_i'(\xi)\psi_j(\xi)\,\mathrm{d}\xi + \frac{v(0)}{2l(0)}q_j(0). \tag{27}$$

The vibratory energy of the models in Fig. 8(a) and (b) is

$$E_v(t) = \tfrac{1}{2}\int_0^{l(t)} [\rho(y_t + vy_x)^2 + Py_x^2 + EIy_{xx}^2]\,\mathrm{d}x \tag{28}$$

and that of the models in Fig. 9(a) and (b) is

$$\begin{aligned} E_v(t) = {} & \tfrac{1}{2}\int_0^{l(t)} [\rho(y_t + vy_x)^2 + Py_x^2 + EIy_{xx}^2]\,\mathrm{d}x \\ & + \tfrac{1}{2}m_e[y_t(l(t),t) + vy_x(l(t),t)]^2 + \tfrac{1}{2}k_e y^2(l(t),t). \end{aligned} \tag{29}$$

The vibratory energy of the models in Figs. 8(c) and 9(c) is given by Eqs. (28) and (29), respectively, with $EI = 0$. Substituting Eqs. (18) and (19) into Eq. (28) yields the discretized expression of the vibratory energy of the models in Fig. 9(a) and (b):

$$E_v(t) = \tfrac{1}{2}[\dot{\mathbf{q}}^{\mathrm{T}}(t)\mathbf{M}(t)\dot{\mathbf{q}}(t) + \dot{\mathbf{q}}^{\mathrm{T}}(t)\mathbf{R}(t)\dot{\mathbf{q}}(t) + \mathbf{q}^{\mathrm{T}}(t)\mathbf{S}(t)\mathbf{q}(t)], \tag{30}$$

where entries of $\mathbf{M}$ are given by Eq. (21)

$$\mathbf{R}_{ij} = -\rho l^{-1}(t)\dot{l}(t)\delta_{ij} + 2\rho l^{-1}(t)\dot{l}(t)\int_0^1 (1-\xi)\psi_i(\xi)\psi_j(\xi)\,\mathrm{d}\xi - m_e l^{-2}(t)\dot{l}(t)\psi_i(1)\psi_j(1), \tag{31}$$

$$\begin{aligned}\mathbf{S}_{ij} = \rho\Big\{ &-\tfrac{1}{4}l^{-2}(t)\dot{l}^2(t)\delta_{ij} + \dot{l}^2(t)l^{-2}(t)\int_0^1 (1-\xi)^2\psi_i'(\xi)\psi_j'(\xi)\,\mathrm{d}\xi \\ &+ l^{-1}(t)[g-\ddot{l}(t)]\int_0^1 (1-\xi)\psi_i'(\xi)\psi_j'(\xi)\,\mathrm{d}\xi\Big\} \\ &+ k_e l^{-1}(t)\psi_i(1)\psi_j(1) \quad + EIl^{-4}(t)\int_0^1 \psi_i''(\xi)\psi_j''(\xi)\,\mathrm{d}\xi \\ &+ m_e l^{-2}(t)[g-\ddot{l}(t)]\int_0^1 \psi_i'(\xi)\psi_j'(\xi)\,\mathrm{d}\xi + \tfrac{1}{4}m_e l^{-1}(t)\dot{l}^2(t)\psi_i(1)\psi_j(1).\end{aligned} \tag{32}$$

The discretized expression of $E_v(t)$ for the model in Fig. 9(c) is given by Eqs. (30)–(32) with $EI = 0$ in Eq. (32). The discretized expression of $E_v(t)$ for the models in Fig. 8(a) and (b) is given by Eqs. (30)–(32) with $m_e = 0$ in the entries of $\mathbf{M}$ and Eq. (31) and with the last term in Eq. (32) set to zero. The discretized expression of $E_v(t)$ for the model in Fig. 8(c) is given by the discretized expression of $E_v(t)$ for the model in Fig. 8(b) with $EI = 0$ in the entries of $\mathbf{S}$. The rate of change of the vibratory energy of each model in Figs. 8 and 9 can be calculated from the control volume and system viewpoints following Refs. [21,23]. The rate of change of $E_v(t)$ from the control volume viewpoint can characterize the dynamic stability of the system under consideration and is obtained by differentiating $E_v(t)$ using Leibnitz's rule. It is given by

$$\begin{aligned}\dot{E}_v(t) = &-\frac{v(t)}{2}EIy_{xx}^2(0,t) - \tfrac{1}{2}\ddot{v}(t)\int_0^{l(t)}[m_e + \rho(l(t)-x)]y_x^2\,\mathrm{d}x \\ &- c_e[y_t(l(t),t) + v(t)y_x(l(t),t)]^2\end{aligned} \tag{33}$$

for the model in Fig. 9(a) and by

$$\begin{aligned}\dot{E}_v(t) = &-\frac{v(t)}{2}[P(0,t) - \rho v^2(t)]y_x^2(0,t) + EIv(t)y_x(0,t)y_{xxx}(0,t) \\ &-\tfrac{1}{2}\ddot{v}(t)\int_0^{l(t)}[m_e + \rho(l(t)-x)]y_x^2\,\mathrm{d}x - c_e[y_t(l(t),t) + v(t)y_x(l(t),t)]^2\end{aligned} \tag{34}$$

for the model in Fig. 9(b). Similarly, $\dot{E}_v(t)$ for the model in Fig. 9(c) is given by Eq. (34) with $EI = 0$ and $\dot{E}_v(t)$ for each model in Fig. 8 is given by that for the corresponding model in Fig. 9 with $c_e = 0$. The discretized expression of $\dot{E}_v(t)$ is

$$\dot{E}_v(t) = \tfrac{1}{2}[\dot{\mathbf{q}}^{\mathrm{T}}(t)\mathbf{F}(t)\dot{\mathbf{q}}(t) + \dot{\mathbf{q}}^{\mathrm{T}}(t)\mathbf{U}(t)\mathbf{q}(t) + \mathbf{q}^{\mathrm{T}}(t)\mathbf{W}(t)\mathbf{q}(t)], \tag{35}$$

where

$$\mathbf{F}_{ij} = -c_e l^{-1}(t)\psi_i(1)\psi_j(1), \quad \mathbf{U}_{ij} = c_e l^{-2}(t)\dot{l}(t)\psi_i(1)\psi_j(1) \tag{36}$$

for the models in Fig. 9, $\mathbf{F}_{ij} = \mathbf{U}_{ij} = 0$ for the models in Fig. 8,

$$\begin{aligned}\mathbf{W}_{ij} = &\tfrac{1}{2}\rho l^{-1}(t)\ddot{v}(t)\int_0^1 \xi\psi_i'(\xi)\psi_j'(\xi)\,\mathrm{d}\xi - \tfrac{1}{2}[m_e + \rho l(t)]l^{-2}(t)\ddot{v}(t)\int_0^1 \psi_i'(\xi)\psi_j'(\xi)\,\mathrm{d}\xi \\ &- \tfrac{1}{4}c_e l^{-3}(t)\dot{l}^2(t)\psi_i(1)\psi_j(1) + EIl^{-5}(t)\dot{l}(t)\psi_i'(0)\psi_j'''(0) \\ &- \tfrac{1}{2}l^{-3}(t)\dot{l}(t)\{[m_e + \rho l(t)][g - \ddot{l}(t)] - \rho\dot{l}^2(t)\}\psi_i'(0)\psi_j'(0)\end{aligned} \tag{37}$$

for the model in Fig. 9(b), $\mathbf{W}_{ij}$ for the model in Fig. 9(c) is given by Eq. (37) with $EI = 0$, $\mathbf{W}_{ij}$ for the model in Fig. 9(a) is given by Eq. (37) with the last two terms replaced with $-\frac{1}{2}EIl^{-5}(t)\dot{l}(t)\psi_i''(0)\psi_j''(0)$, and $\mathbf{W}_{ij}$ for each model in Fig. 8 is given by that for the corresponding model in Fig. 9 with $c_e = 0$.

3.2. Results and discussion

The parameters used here are the same as those in Section 2.2. Under the upward movement profile shown in Fig. 10 [23], where $l(0)$ equals l in Section 2.2, and the same initial conditions as those for the corresponding stationary cable models, the undamped (i.e., $c_e = 0$) responses of the models in Figs. 8 and 9 are calculated with $n = 30$ and shown in Figs. 11 and 12, respectively. The responses of the models in Figs. 8 and 9 are virtually indistinguishable within the scales of the plots in Figs. 11 and 12, respectively. The vibratory energies of the models in Fig. 9 are smaller than those of the models in Fig. 8 and approach them when k_e approaches infinity (e.g., $k_e = 200,000\ \mathrm{N/m}$).

The transverse force at any point other than the fixed ends of the models in Figs. 8(a) and 9(a) and the lower end of the model in Fig. 9(c) can be calculated. The discretized expression of $\dot{E}_v(t)$ for the model in Fig. 8(c) yield essentially the same result as that obtained from $E_v(t)$ through finite difference (not shown). The discretized expressions of $\dot{E}_v(t)$ for the models in Figs. 8(a) and

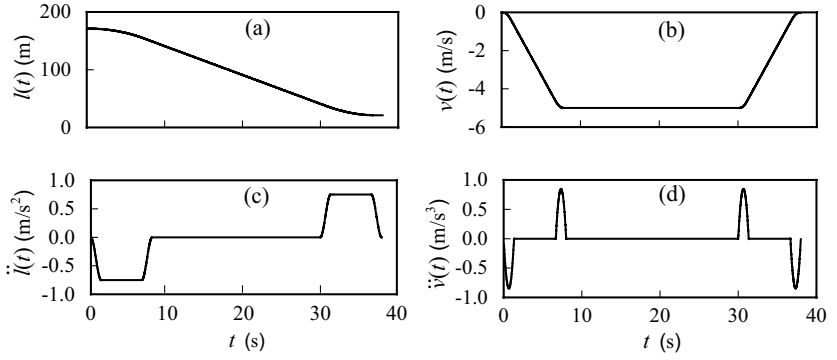

Fig. 10. Upward movement profile of the hoist cable: (a) $l(t)$, (b) $v(t)$, (c) $\ddot{l}(t)$, and (d) $\ddot{v}(t)$.

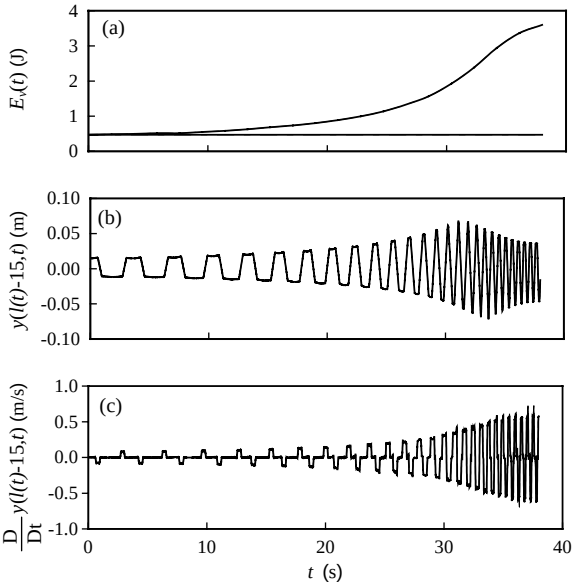

Fig. 11. The undamped responses of the models in Fig. 8: (a) vibratory energy, (b) displacement of a fixed particle at $x = l(t) - 15$ m, and (c) velocity of a fixed particle at $x = l(t) - 15$ m, $Dy(l(t) - 15, t)/Dt$. The horizontal lines in (a) show the energies of the stationary cable models in Fig. 1. Dashed lines, Figs. 8(a) and 1(a); dash–dotted lines, Figs. 8(b) and 1(b); solid lines, Figs. 8(c) and 1(c).

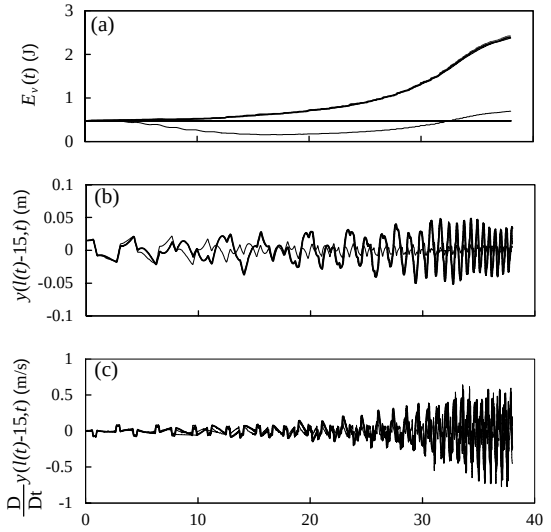

Fig. 12. The undamped responses of the models in Fig. 9 along with the response of the model in Fig. 9(a) under the optimal suspension stiffness and damping coefficient: (a)–(c) as in Fig. 11. The horizontal lines in (a) show the energies of the stationary cable models in Fig. 2. Dashed lines, Figs. 9(a) and 2(a); dash–dotted lines, Figs. 9(b) and 2(b); thick solid lines, Figs. 9(c) and 2(c). The response of the model in Fig. 9(a) under k^* and c^* is shown in thin solid lines in (a)–(c).

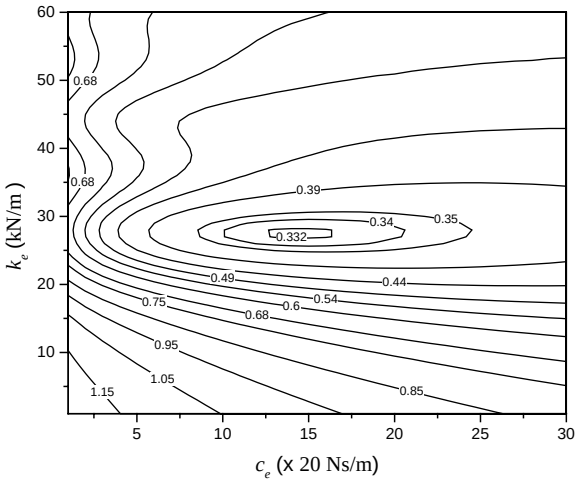

Fig. 13. Contour plot of the average vibratory energy of the model in Fig. 9(a) where its isoline values in J are labelled. In all the calculations $n = 30$.

9(a) cannot be used here because $y''_{xx}(0,t)$ cannot be determined with the untensioned beam eigenfunctions. As the second term in Eq. (34) has a much smaller amplitude than the first term, the discretized expressions of $\dot{E}_v(t)$ for the models in Figs. 8(b) and 9(b) yield essentially the same results as those obtained from the corresponding $E_v(t)$ through finite difference. While the discretized expression of $\dot{E}_v(t)$ for the model in Fig. 9(c) can be used when $c_e = 0$, it cannot be used when $c_e \neq 0$ because $y_x(l(t),t)$ cannot be determined with the trial functions satisfying $\phi_{jx}(l(t),t) = 0$.

Under the above initial conditions and movement profile the dependence of the average vibratory energy of the model in Fig. 9(a), defined by $\bar{E}_v = (1/t_f)\int_0^{t_f} E_v(t)\,\mathrm{d}t$, where $t_f = 38$ s, on k_e and c_e with the other parameters unchanged is shown in Fig. 13. With the optimal suspension stiffness and damping coefficient around $k_e^* = 2800$ N/m and $c_e^* = 280$ N s/m, respectively, $\bar{E}_v$ is reduced from 1.22 J for the models in Fig. 8 to 0.33 J. The response of the model in Fig. 9(a) under k_e^* and c_e^* is shown in thin solid lines in Fig. 12. The optimal suspension stiffness and damping coefficient are generally independent of the initial conditions. It is interesting to find that the vibratory energy of the models in Fig. 9 with $k_e = c_e = 0$ is essentially the same as that of the models in Fig. 8.

4. Conclusions

While the string and beam models predict essentially the same gross behaviors for the stationary and moving hoist cables, the maximum bending moment occurs at the fixed ends of the beam models. The untensioned beam eigenfunctions cannot be used here to determine y_{xx} and y_{xxx} at the fixed ends of the beam models. With the optimal suspension stiffness and damping coefficient the average vibratory energy of the models in Fig. 9 during upward movement is reduced from that of the models in Fig. 8 by over 70%.

Acknowledgements

This material is based on work supported by the National Science Foundation through award number CMS-0116425.

Appendix A. Trial functions

The eigenfunctions of a fixed–fixed beam of length l under uniform tension T are

$$\phi_j(x) = B_j\{\cos\beta_{1j}x - \frac{\sigma_j}{\gamma_j}\sin\beta_{1j}x - \frac{1}{\gamma_j}[(\beta_{2j}\sin\beta_{1j}l - \beta_{1j}\cos\beta_{1j}l)e^{\beta_{2j}(x-l)} + (\beta_{2j}\sin\beta_{1j}l + \beta_{1j}\cos\beta_{1j}l)e^{-\beta_{2j}(x+l)} - \beta_{1j}(e^{-\beta_{2j}x} - e^{-\beta_{2j}(2l-x)})]\}, \tag{A.1}$$

where B_j are determined from the normalization relations $\int_0^l \phi_j^2(x)\,dx = 1$,

$$\gamma_j = 2\beta_{2j}e^{-\beta_{2j}l}\sin\beta_{1j}l - \beta_{1j}(1 - e^{-2\beta_{2j}l}), \quad \sigma_j = 2\beta_{2j}e^{-\beta_{2j}l}\cos\beta_{1j}l - \beta_{2j}(1 + e^{-2\beta_{2j}l}), \tag{A.2}$$

$$\beta_{1j} = \sqrt{\frac{\sqrt{T^2 + 4EI\rho\Omega_j^2} - T}{2EI}}, \quad \beta_{2j} = \sqrt{\frac{\sqrt{T^2 + 4EI\rho\Omega_j^2} + T}{2EI}}, \tag{A.3}$$

in which Ω_j are obtained from the frequency equation

$$4\beta_{1j}\beta_{2j}\,e^{-\beta_{2j}l} - 2\beta_{1j}\beta_{2j}\,(1 + e^{-2\beta_{2j}l})\cos\beta_{1j}l + (\beta_{2j}^2 - \beta_{1j}^2)\,(1 - e^{-2\beta_{2j}l})\sin\beta_{1j}l = 0. \tag{A.4}$$

When $T = 0$, $\beta_{1j} = \beta_{2j} = \beta_j$ with $\beta_j l$ being the jth positive root z_j of

$$2e^{-z_j} - (1 + e^{-2z_j})\cos z_j = 0. \tag{A.5}$$

The trial functions for the models in Fig. 1(b) and (c) are $\phi_j(x) = \sqrt{2/l}\sin(j\pi x/l)$.

The eigenfunctions of a fixed–free beam of length l under uniform tension T are

$$\phi_j(x) = B_j\{\cos\beta_{1j}x - \frac{\sigma_j}{\gamma_j}\sin\beta_{1j}x + \frac{1}{\gamma_j}[\beta_{1j}^2(\cos\beta_{1j}l - \sin\beta_{1j}l)e^{\beta_{2j}(x-l)} - \beta_{1j}^2(\cos\beta_{1j}l + \sin\beta_{1j}l)e^{-\beta_{2j}(x+l)} - \beta_{2j}^2(e^{-\beta_{2j}x} - e^{-\beta_{2j}(2l-x)})]\}, \tag{A.6}$$

where B_j are determined through normalization,

$$\gamma_j = 2\beta_{1j}^2e^{-\beta_{2i}l}\sin\beta_{1i}l + \beta_{2i}^2(1 - e^{-2\beta_{2i}l}), \quad \sigma_j = 2\beta_{1j}^2e^{-\beta_{2j}l}\cos\beta_{1j}l + \beta_{2j}^2(1 + e^{-2\beta_{2i}l}), \tag{A.7}$$

and β_{1j} and β_{2j} are defined in Eq. (A.3) with Ω_j obtained from the frequency equation

$$2e^{-\beta_{2j}l}[\beta_{1j}^3(T + EI\beta_{1j}^2) - \beta_{2j}^3(T - EI\beta_{2j}^2)] + [T(\beta_{2j} - \beta_{1j}) + EI\beta_{1j}\beta_{2j}(\beta_{2j} + \beta_{1j})](1 + e^{-2\beta_{2j}l}) \times \beta_{1j}\beta_{2j}\cos\beta_{1j}l + [T(\beta_{1j} + \beta_{2j}) + EI\beta_{1j}\beta_{2j}(\beta_{1j} - \beta_{2j})](1 - e^{-2\beta_{2j}l})\beta_{1j}\beta_{2j}\sin\beta_{1j}l = 0. \tag{A.8}$$

When $T = 0$, $\beta_{1j} = \beta_{2j} = \beta_j$ with $\beta_j l$ being the jth positive root z_j of

$$2e^{-z_j} + (1 + e^{-2z_j})\cos z_j = 0. \tag{A.9}$$

The eigenfunctions of a pinned–free beam of length l under uniform tension T are

$$\phi_j(x) = B_j\left\{\sin\beta_{1j}x + \frac{\beta_{1j}^2\sin\beta_{1j}l}{\beta_{2j}^2(1-\mathrm{e}^{-2\beta_{2j}l})}[\mathrm{e}^{\beta_{2j}(x-l)} - \mathrm{e}^{-\beta_{2j}(x+l)}]\right\}, \tag{A.10}$$

where B_j are determined through normalization and β_{1j} and β_{2j} are defined in Eq. (A.3) with Ω_j obtained from the frequency equation

$$\beta_{1j}(T - EI\beta_{2j}^2)(1+\mathrm{e}^{-2\beta_{2j}l})\sin\beta_{1j}l + \beta_{2j}(T + EI\beta_{1j}^2)(1-\mathrm{e}^{-2\beta_{2j}l})\cos\beta_{1j}l = 0. \tag{A.11}$$

When $T = 0$, $\phi_j(x)$ for $j \geqslant 2$ are given by Eq. (A.1), where $\beta_{1j} = \beta_{2j} = \beta_j$ with $\beta_j l$ being the $(j-1)$th positive root z_{j-1} of

$$(1-\mathrm{e}^{-2z_j})\cos z_j - (1+\mathrm{e}^{-2z_j})\sin z_j = 0. \tag{A.12}$$

The normalized eigenfunction for the rigid-body mode is $\phi_1(x) = \sqrt{3/l^3}\,x$. The trial functions for the model in Fig. 2(c) are $\phi_j(x) = \sqrt{2/l}\sin[(2j-1)\pi x/2l]$.

The functions $\psi_j(\xi)$ for the model in Fig. 8(a) are

$$\psi_j(\xi) = B_j\{\cos\kappa_j\pi\xi - \frac{\theta_j}{\lambda_j}\sin\kappa_j\pi\xi - \frac{1}{\lambda_j}[\mathrm{e}^{-\kappa_j\pi(1-\xi)}(\sin\kappa_j\pi - \cos\kappa_j\pi) + \mathrm{e}^{-\kappa_j\pi(1+\xi)}(\sin\kappa_j\pi + \cos\kappa_j\pi) - \mathrm{e}^{-\kappa_j\pi\xi} + \mathrm{e}^{-\kappa_j\pi(2-\xi)}]\}, \tag{A.13}$$

where $\kappa_j\pi$ is the jth positive root z_j of Eq. (A.5) and

$$\lambda_j = 2\mathrm{e}^{-\kappa_j\pi}\sin\kappa_j\pi - 1 + \mathrm{e}^{-2\kappa_j\pi}, \quad \theta_j = 2\mathrm{e}^{-\kappa_j\pi}\cos\kappa_j\pi - 1 - \mathrm{e}^{-2\kappa_j\pi}. \tag{A.14}$$

The functions $\psi_j(\xi)$ for the model in Fig. 9(a) are

$$\psi_j(\xi) = B_j\{\cos\kappa_j\pi\xi - \frac{\theta_j}{\lambda_j}\sin\kappa_j\pi\xi - \frac{1}{\lambda_j}[\mathrm{e}^{-\kappa_j\pi(1-\xi)}(\sin\kappa_j\pi - \cos\kappa_j\pi) + \mathrm{e}^{-\kappa_j\pi(1+\xi)}(\sin\kappa_j\pi + \cos\kappa_j\pi) + \mathrm{e}^{-\kappa_j\pi\xi} - \mathrm{e}^{-\kappa_j\pi(2-\xi)}]\}, \tag{A.15}$$

where $\kappa_j\pi$ is the jth positive root z_j of Eq. (A.9) and

$$\lambda_j = 2\mathrm{e}^{-\kappa_j\pi}\sin\kappa_j\pi + 1 - \mathrm{e}^{-2\kappa_j\pi}, \quad \theta_j = 2\mathrm{e}^{-\kappa_j\pi}\cos\kappa_j\pi + 1 + \mathrm{e}^{-2\kappa_j\pi}. \tag{A.16}$$

The constants B_j in Eqs. (A.13) and (A.15) are both expressed as

$$B_j = \sqrt{\kappa_j\pi}\left\{\left[1+\left(\frac{\theta_j}{\lambda_j}\right)^2\right][\tfrac{1}{4}\sinh 2\kappa_j\pi - \cosh\kappa_j\pi\sin\kappa_j\pi] + \left[1-\left(\frac{\theta_j}{\lambda_j}\right)^2\right][\tfrac{1}{4}\sin 2\kappa_j\pi - \sinh\kappa_j\pi\cos\kappa_j\pi] + \kappa_j\pi + 2\frac{\theta_j}{\lambda_j}[\tfrac{1}{4}(\cos 2\kappa_j\pi - \cosh 2\kappa_j\pi) + \sin\kappa_j\pi\sinh\kappa_j\pi]\right\}^{-1/2}. \tag{A.17}$$

Calculation shows that $B_j = 1$. The functions $\psi_j(\xi)(j \geqslant 2)$ for the model in Fig. 9(b) are

$$\psi_j(\xi) = B_j\{\sin\kappa_j\pi\xi + \frac{\sin\kappa_j\pi}{1-\mathrm{e}^{-2\kappa_j\pi}}[\mathrm{e}^{\kappa_j\pi(\xi-1)} - \mathrm{e}^{-\kappa_j\pi(\xi+1)}]\}, \tag{A.18}$$

where $\kappa_j\pi$ is the $(j-1)$th positive root z_{j-1} of Eq. (A.12) and

$$B_j = \sqrt{\frac{2(1-\mathrm{e}^{-2\kappa_j\pi})^2}{(1-\mathrm{e}^{-2\kappa_j\pi})^2 - 4\mathrm{e}^{-2\kappa_j\pi}\sin^2\kappa_j\pi}}. \tag{A.19}$$

The associated function for the rigid-body mode is $\psi_1(\xi) = \sqrt{3}\xi$. For the models in Fig. 8(b) and (c), $\psi_j(\xi) = \sqrt{2}\sin\pi j\xi$, and for the model in Fig. 9(c), $\psi_j(\xi) = \sqrt{2}\sin[(2j-1)\pi\xi/2]$. Since a large number of terms are used in Eqs. (6) and (18), to avoid loss of precision in evaluating the hyperbolic functions with large arguments, the trial functions are expressed above as exponential functions with negative exponents.

Appendix B. Initial displacements

The static deflection of a fixed–fixed beam of length l under uniform tension $m_e g$, subjected to a concentrated force P at $x = a$, is

$$Y(x) = \begin{cases} A_1 + N_1 x + Q_1(x), & 0 < x < a, \\ A_2 + N_2 x + Q_2(x), & a < x < l, \end{cases} \tag{B.1}$$

where

$$\begin{aligned} A_1 = \alpha[&-2sa\mathrm{e}^{-sl} + sl(\mathrm{e}^{-sa} + \mathrm{e}^{-2sl+sa}) - (\mathrm{e}^{-sa} - \mathrm{e}^{-2sl+sa}) + 1 - \mathrm{e}^{sa-sl} \\ &- \mathrm{e}^{-2sl} + \mathrm{e}^{-sa-sl} - s(l-a)(1+\mathrm{e}^{-2sl})], \end{aligned}$$

$$N_1 = \alpha s[2\mathrm{e}^{-sl} - \mathrm{e}^{-sa} - \mathrm{e}^{-2sl+sa} + s(l-a)(1-\mathrm{e}^{-2sl}) - 1 - \mathrm{e}^{-2sl} + \mathrm{e}^{sa-sl} + \mathrm{e}^{-sa-sl}],$$

$$\begin{aligned} Q_1(x) = \alpha[&-(1-sa)\mathrm{e}^{-sl+sx} + \mathrm{e}^{-sa+sx} - 0.5sl(\mathrm{e}^{-sa+sx} + \mathrm{e}^{-2sl+sa+sx}) \\ &+\mathrm{e}^{-2sl+sx} - \mathrm{e}^{-sa-sl+sx} + s(l-a)\mathrm{e}^{-2sl+sx} + sa\mathrm{e}^{-sl-sx} - 0.5sl\mathrm{e}^{-sa-sx} \\ &+ (1.5sl-1)\mathrm{e}^{-2sl+sa-sx} - \mathrm{e}^{-sx} + s(l-a)\mathrm{e}^{-sx}], \end{aligned} \tag{B.2}$$

$$\begin{aligned} A_2 = \alpha[&sl(\mathrm{e}^{-sa} + \mathrm{e}^{-2sl+sa}) - \mathrm{e}^{-sa} + \mathrm{e}^{-2sl+sa} - s(l+a)(1+\mathrm{e}^{-2sl}) + (s^2la+1)(1-\mathrm{e}^{-2sl}) \\ &- \mathrm{e}^{sa-sl} - \mathrm{e}^{-sa-sl} + 2sa\mathrm{e}^{-sl}], \end{aligned}$$

$$N_2 = \alpha s[-\mathrm{e}^{-sa} - \mathrm{e}^{-2sl+sa} + 1 + \mathrm{e}^{-2sl} + \mathrm{e}^{sa-sl} + \mathrm{e}^{-sa-sl} - sa(1-\mathrm{e}^{-2sl}) - 2\mathrm{e}^{-sl}],$$

$$\begin{aligned} Q_2(x) = \alpha[&\mathrm{e}^{-sa-sl+sx} + \mathrm{e}^{-2sl+sx} - \mathrm{e}^{-sl+sx} + sa\mathrm{e}^{-sl+sx} - 0.5sl\mathrm{e}^{-2sl+sa+sx} - (1+0.5sl)\mathrm{e}^{-sa-2sl+sx} \\ &+ s(l-a)\mathrm{e}^{-2sl+sx} - \mathrm{e}^{sa-sl-sx} - \mathrm{e}^{-sx} + \mathrm{e}^{-sl-sx} + sa\mathrm{e}^{-sl-sx} - 0.5sl\mathrm{e}^{-sa-sx} \\ &- (0.5sl-1)\mathrm{e}^{sa-sx} + s(l-a)\mathrm{e}^{-sx}], \end{aligned} \tag{B.3}$$

in which

$$s = \sqrt{\frac{m_e g}{EI}}, \quad \alpha = \frac{P}{EIs^3[4\mathrm{e}^{-sl} - 2(1+\mathrm{e}^{-2sl}) + sl(1-\mathrm{e}^{-2sl})]}. \tag{B.4}$$

The static deflection of a pinned–pinned beam of length l under uniform tension $m_e g$, subjected to a concentrated force P at $x = a$, is given by Eq. (B.1) with

$$A_1 = 0, \quad N_1 = \frac{P(l-a)}{EIs^2 l},$$

$$Q_1(x) = \frac{P}{2EIs^3(-1+e^{-2sl})}(e^{-sa+sx} + e^{-2sl+sa+sx} - e^{-sa-sx} - e^{-2sl+sa-sx}), \tag{B.5}$$

$$A_2 = \frac{Pa}{EIs^2}, \quad N_2 = -\frac{Pa}{EIs^2 l},$$

$$Q_2(x) = \frac{P}{2EIs^3(-1+e^{-2sl})}(e^{-2sl+sa+sx} + e^{-sa-2sl+sx} - e^{sa-sx} + e^{-sa-sx}). \tag{B.6}$$

Under a unit force (i.e., $p = 1$) at $x = a$ the displacement at the same point, denoted by Y_f and Y_p for the two cases, can be calculated from the above expressions. The initial displacement for the models in Figs. 1(a) and 2(a) is given by Eqs. (B.1)–(B.3) with $P = d/Y_f$ and that for the models in Figs. 2(a) and 2(b) is given by Eqs. (B.1), (B.5) and (B.6) with $P = d/Y_p$. The initial displacement for the models in Figs. 1(c) and 2(c) is

$$y(x,0) = \begin{cases} \dfrac{xd}{a}, & 0 \leqslant x \leqslant a, \\ \dfrac{(l-x)d}{l-a}, & a \leqslant x \leqslant l. \end{cases} \tag{B.7}$$

References

[1] N.J. Gimsing, Cable Supported Bridges, 2nd Edition, Wiley, New York, 1997.

[2] R.M. Chi, H.T. Shu, Longitudinal vibration of a hoist rope coupled with the vertical vibration of an elevator car, Journal of Sound and Vibration 148 (1) (1991) 154–159.

[3] P. Hagedorn, On the computation of a damped wind-excited vibrations of overhead transmission lines, Journal of Sound and Vibration 83 (2) (1982) 253–271.

[4] D.R. Yoerger, M.A. Grosenbaugh, M.S. Triantafyllou, J.J. Burgess, Drag forces and flow-induced vibrations of a long vertical tow cable. Part I. Steady-state towing conditions, Journal of Offshore Mechanics and Arctic Engineering 113 (2) (1991) 117–127.

[5] H.M. Irvine, T.K. Caughey, The linear theory of free vibrations of a suspended cable, Proceedings of the Royal Society, London, A 341 (1974) 299–315.

[6] M.S. Triantafyllou, The dynamics of taut inclined cables, Quarterly Journal of Mechanics and Applied Mathematics 37 (1984) 421–440.

[7] S.S. Sergev, W.D. Iwan, The natural frequencies and mode shapes of cables with attached masses, American Society of Mechanical Engineers Journal of Energy Resources and Technology 103 (1981) 237–242.

[8] S.P. Cheng, N.C. Perkins, Closed-form vibration analysis of sagged cable/mass suspensions, American Society of Mechanical Engineers Journal of Applied Mechanics 59 (1992) 923–928.

[9] A. Simpson, On the oscillatory motions of translating elastic cables, Journal of Sound and Vibration 20 (1972) 177–189.

[10] M.S. Triantafyllou, Dynamics of translating cables, Journal of Sound and Vibration 103 (2) (1985) 171–182.

[11] N.C. Perkins, C.D. Mote Jr., Three-dimensional vibration of traveling elastic cables, Journal of Sound and Vibration 114 (2) (1987) 325–340.

[12] J.A. Wickert, C.D. Mote Jr., Traveling load response of an axially moving string, Journal of Sound and Vibration 149 (1991) 267–284.

[13] W.D. Zhu, C.D. Mote Jr., Free and forced response of an axially moving string transporting a damped linear oscillator, Journal of Sound and Vibration 177 (1994) 591–610.

[14] M.S. Triantafyllou, G.S. Triantafyllou, The paradox of the hanging string an: explanation using singular perturbation, Journal of Sound and Vibration 148 (2) (1991) 343–351.

[15] J.J. Burgess, Bending stiffness in a simulation of undersea cable deployment, International Journal of Offshore and Polar Engineering 3 (3) (1993) 197–204.
[16] M.S. Dhotarad, N. Ganesan, B.V.A. Rao, Transmission line vibration with 4R dampers, Journal of Sound and Vibration 60 (4) (1978) 604–606.
[17] M. Irvine, Local bending stresses in cables, International Journal of Offshore and Polar Engineering 3 (3) (1993) 172–175.
[18] R. Roberts, Control of high-rise/high-speed elevators, Proceedings of the American Control Conference, Philadelphia, FM16-1, 1998.
[19] T. Yamamoto, K. Yasuda, M. Kato, Vibrations of a string with time-variable length, Bulletin of the Japan Society of Mechanical Engineers 21 (162) (1978) 1677–1684.
[20] Y. Terumichi, M. Ohtsuka, M. Yoshizawa, Y. Fukawa, Y. Tsujioka, Nonstationary vibrations of a string with time-varying length and a mass–spring system attached at the lower end, Nonlinear Dynamics 12 (1997) 39–55.
[21] W.D. Zhu, J. Ni, Energetics and stability of translating media with an arbitrarily varying length, American Society of Mechanical Engineers Journal of Vibration and Acoustics 122 (2000) 295–304.
[22] W.D. Zhu, L.J. Teppo, Design and analysis of a scaled model of a high-rise, high-speed elevator, Journal of Sound and Vibration, in press. XRef: 10.1016S0022460X0201210X
[23] W.D. Zhu, Control volume and system formulations for translating media and stationary media with moving boundaries, Journal of Sound and Vibration 254 (1) (2002) 189–201.